

Itinerant topological magnons and spin excitons in twisted transition metal dichalcogenides: Mapping electron topology to spin counterpart

Wei-Tao Zhou,^{1,*} Zhao-Yang Dong,^{2,*} Zhao-Long Gu,^{1,3,†} and Jian-Xin Li^{1,3,‡}

¹*National Laboratory of Solid State Microstructures and Department of Physics, Nanjing University, 210093 Nanjing, China*

²*Department of Applied Physics, Nanjing University of Science and Technology, Nanjing 210094, China*

³*Collaborative Innovation Center of Advanced Microstructures, Nanjing University, 210093 Nanjing, China*

(Dated: February 18, 2025)

Twisted transition metal dichalcogenides (tTMDs) provide a highly tunable platform to explore the interplay between strong correlation and topology. Among them, the properties involving the charge degree of freedom have been extensively studied, while those related to spin are much less investigated. Motivated by the recent discovery of integer and fractional quantum anomalous Hall effects in tMoTe₂, where the flat-band ferromagnetism is one of the essential prerequisites, we investigate theoretically the spin excitations out of the flat-band ferromagnetic ground state in tMoTe₂. Remarkably, we identify the itinerant magnons and spin excitons with nontrivial topology. We elaborate that the topology of these itinerant spin excitations, which are described as particle-hole bound states, inherits directly from that of the underlying electrons and is essentially different from that in local spin systems. Thus, we establish a direct relationship of the topology between the many-body excitations and their fundamental constituents. We further demonstrate that by tuning the displacement field, a topological transition for both the magnon and spin exciton happens, leading to a step-like change and bifurcation in the thermal Hall conductance, which could serve as unique and compelling evidence to be tested experimentally.

tTMD moiré materials have emerged as a simple yet rich model system to study exotic phenomena, such as Mott insulators [1–3], generalized Wigner crystals [1, 4–6], unconventional superconductors [7, 8], the Kondo effect [9, 10] and many other correlated states of matter [11–18]. The intertwined correlation and nontrivial band topology have further induced the integer and fractional quantum anomalous Hall effects [19–24]. In such cases, the tunable moiré flat bands stabilize itinerant ferromagnetism due to spontaneous spin polarization, which is a prerequisite for the emergence of quantum anomalous Hall effects. Despite being universal and important in tTMD materials, the itinerant ferromagnetism, and especially its spin excitations, have rarely been investigated.

The spin excitations in local spin systems have been formally studied by linear spin wave theory (LSWT), which maps the motion of a single spin-flip excitation—magnon into a bosonic model. The topology of magnons

has been elaborated to be induced by the Dzyaloshinskii–Moriya interaction, which effectively acts to add a flux generated by the magnon hoppings resembling that in the famous Haldane model [25–34]. On the contrary, the investigations on the itinerant magnons have been limited to toy models [35–40] and their topological character has remained elusive due to the lack of an effective set of bases for itinerant magnons. In this work, we propose the realization of itinerant topological magnons in the realistic tMoTe₂ system, whose topology can be tuned by applying a displacement field. By describing the itinerant magnons as particle-hole bound states and introducing a magnetic effective model, we point out that the origin of the nontrivial topology of itinerant magnons is directly inherited from that of the underlying electronic band, which is essentially different from the situation in local spin systems. Moreover, we find itinerant topological spin excitons in a range of twist angles and elaborate that they originate from the split of the particle-hole bound states by the gap between the electronic bands. We further suggest that the itinerant magnons and spin excitons can be experimentally verified by spectral measurement and the topological transition of magnons can also be probed by an abrupt change of thermal Hall conductance. Our work deepens the understanding of spin excitations in itinerant electron systems with flat bands and paves the way towards future experimental investigation of spintronics in tTMDs.

Electronic Model

We start with the continuum model of tTMD, in which the low-energy band structure is described by the topmost valence bands of the two monolayers at $\pm K_{b,t}$ points [see Fig. 1(a) and (b)], modulated by the moiré potential and interlayer tunneling [41–43]. Due to the large spin-orbit coupling, these topmost valence bands exhibit quadratic dispersion resembling that of a free electron with a modified mass and are spin-valley locked. Since the $\pm K$ valleys are decoupled due to large momentum transfer while related by time-reversal symmetry, we focus on $+K$ valley (spin- \uparrow block), of which the moiré Hamiltonian is given by

$$\mathcal{H}_{\uparrow} = \begin{pmatrix} -\frac{\hbar^2(\mathbf{k}-\boldsymbol{\kappa}_+)^2}{2m^*} + \Delta_+(\mathbf{r}) & \Delta_T(\mathbf{r}) \\ \Delta_T^\dagger(\mathbf{r}) & -\frac{\hbar^2(\mathbf{k}-\boldsymbol{\kappa}_-)^2}{2m^*} + \Delta_-(\mathbf{r}) \end{pmatrix}. \quad (1)$$

This matrix is defined in the layer bases. m^* is the effective

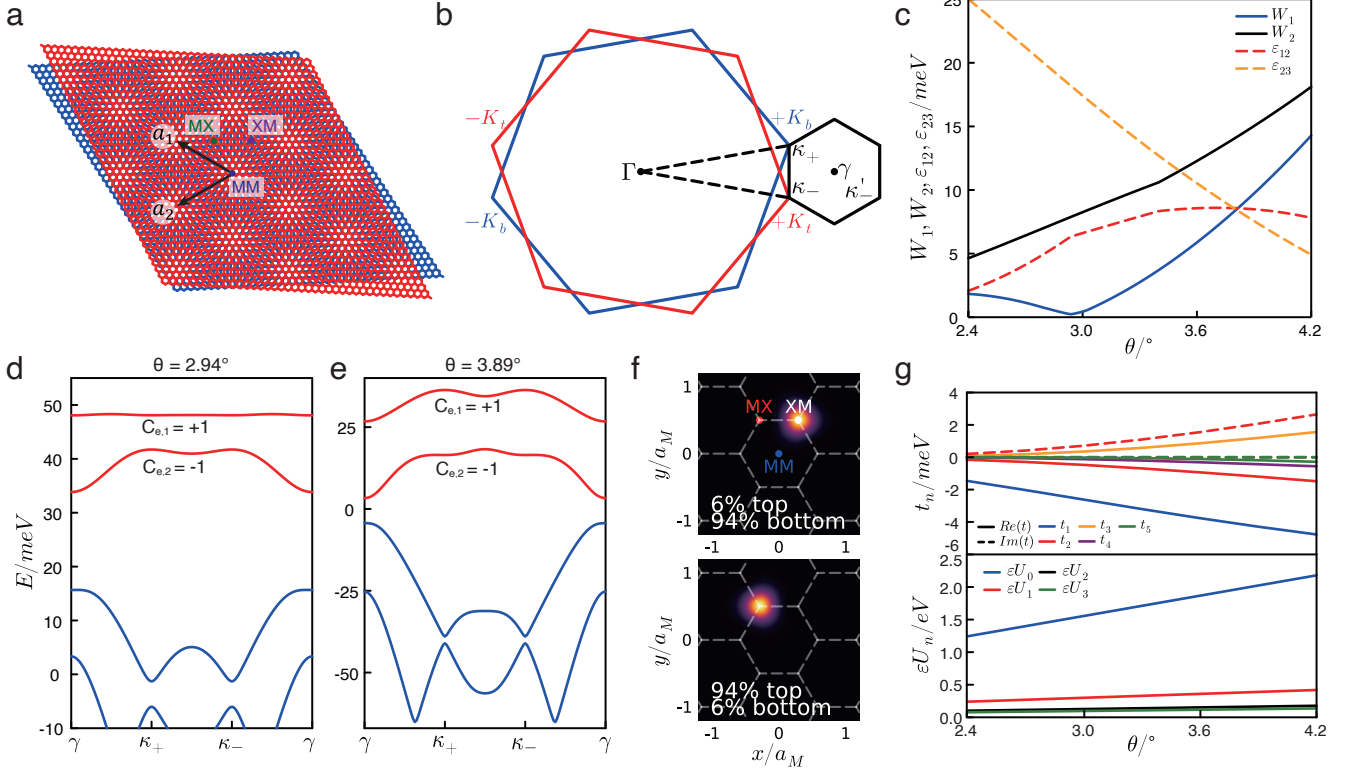


FIG. 1. **Moiré superlattice and tight-binding model.** **a**, Moiré superlattice. a_1, a_2 are moiré superlattice vectors. MM, MX, XM are high symmetry stacking regions. **b**, Brillouin zones of the top (red) and bottom (blue) monolayer and the moiré Brillouin zone (black). **c**, Widths of the topmost two bands W_1, W_2 and the first two band gaps $\varepsilon_{12}, \varepsilon_{23}$. **d, e**, Moiré band structure at $\theta = 2.94^\circ$ and $\theta = 3.89^\circ$, respectively. The topmost two bands in both cases have nonzero Chern numbers ± 1 . **f**, Two generated Wannier states at $\theta = 2.94^\circ$, which center at XM, MX stacking regions and show large layer polarization. **g**, Exactly calculated hopping parameters and gate-screened interacting strengths.

tive mass of an electron. The layer-dependent momentum offset κ_{\pm} captures the rotation of the two monolayers in the momentum space, as shown in Fig. 1(b). Δ_{\pm}, Δ_T are the moiré potential and interlayer tunneling, respectively. Constrained by the space group D_3 and time-reversal symmetry \mathcal{T} of tTMD, Δ_{\pm}, Δ_T can be parameterized by

$$\Delta_{\pm}(\mathbf{r}) = 2V \sum_{j=1,3,5} \cos(\mathbf{g}_j \cdot \mathbf{r} \pm \psi), \quad (2)$$

$$\Delta_T(\mathbf{r}) = w(1 + e^{i\mathbf{g}_2 \cdot \mathbf{r}} + e^{i\mathbf{g}_3 \cdot \mathbf{r}}), \quad (3)$$

where $\mathbf{g}_1 = (4\pi/\sqrt{3}a_M, 0)$ (a_M is the moiré lattice constant) and \mathbf{g}_j with $j = 2, 3, \dots, 6$ are related to \mathbf{g}_1 by $(j-1)\pi/3$ rotation. Both Δ_{\pm} and Δ_T are truncated to the lowest harmonic order, which is sufficient to capture the low-energy electron bands. When applying displacement field V_z , Δ_{\pm} is replaced by $\Delta_{\pm} \pm V_z/2$. (V, ψ, w) specify the strength and distribution of moiré potential as well as the strength of interlayer tunneling. Here we take m^* to be $0.6m_0$ (m_0 is the mass of a free electron)

and (V, ψ, w) to be $(20.8\text{meV}, 107.7^\circ, -23.8\text{meV})$, which are from a large-scale first-principles calculation of AA-stacked tMoTe₂ [44].

In Fig. 1(c), we present the electronic band widths and gaps derived by the continuum model. It shows that the first band reaches extreme flatness at 2.94° , which serves as the magic angle in tTMD [43, 45] and resembles that in twisted bilayer graphene [46–49]. In the following, we focus on the 2.94° case and choose a commensurate twist angle 3.89° as a comparison. In Fig. 1(d) and (e), we show the electron band structures in the two cases, of which the first two bands have nonzero Chern numbers ± 1 and are separated from the rest of the spectrum. We generate an effective tight-binding model by constructing two layer-polarized Wannier states which emerge as an effective honeycomb lattice as shown in Fig. 1(f), and the exactly calculated hopping parameters and interactions are shown in Fig. 1(g). The effective electronic model can be well captured by a nearest hopping t_1 , next-nearest hopping t_2 with spin-dependent $\pm 2\pi/3$ phase and an on-site Hubbard interaction U , which is right the Kane-Mele

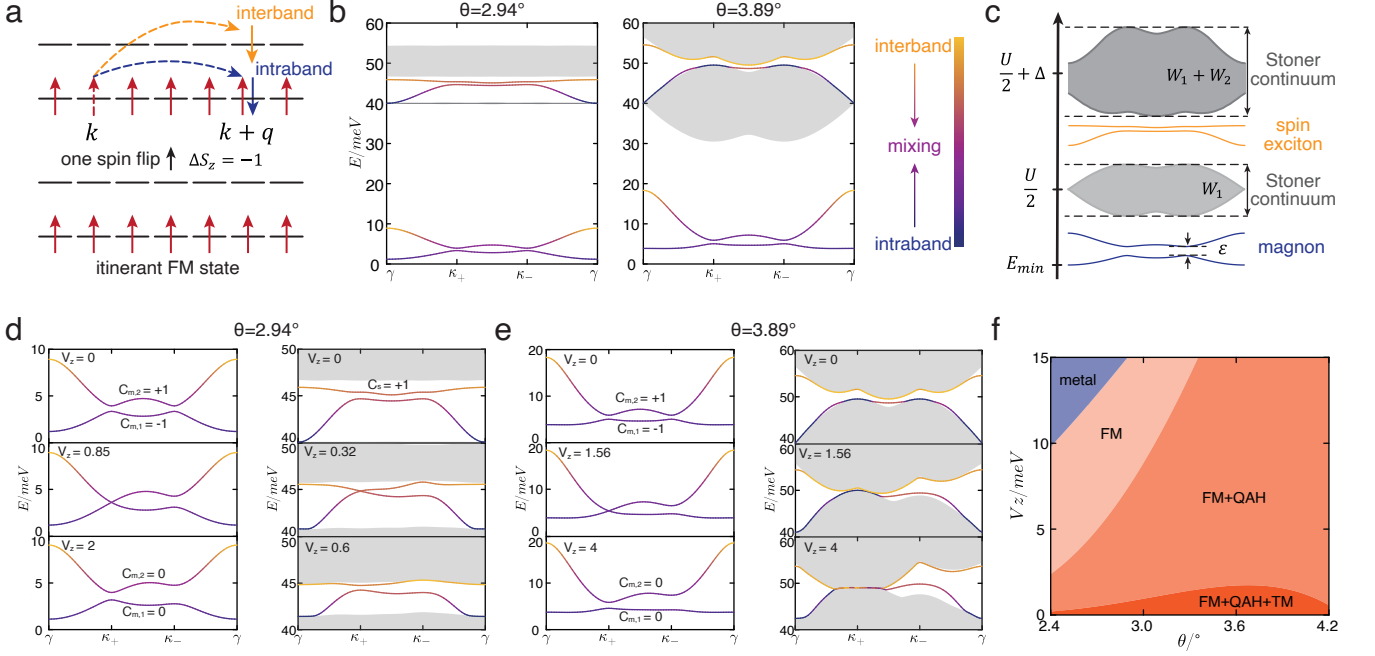


FIG. 2. **Spin excitations out of the itinerant FM state.** **a**, Schematic of the itinerant FM ground state, and the intraband and interband spin-flip particle-hole excitations. **b**, Spectra of spin excitations at $\theta = 2.94^\circ$ (left) and $\theta = 3.89^\circ$ (right) without a displacement field. The color of magnons and spin excitons represents the component of the intraband and interband spin flips. **c**, Schematic of the typical energy band for spin excitations, which is divided into magnons, spin excitons and Stoner continua. $U, \Delta, W_{1,2}$ denote the Hubbard interaction, average gap between the topmost two electron bands and widths of the two electron bands, respectively. **d, e**, Evolution of magnons (left) and spin excitons (right) at $\theta = 2.94^\circ$ and $\theta = 3.89^\circ$ by varying V_z . **f**, Phase diagram with respect to twist angle and displacement field V_z . All results in **b, d, e, f** are obtained at $U = 80$ meV.

model [50, 51] with the Hubbard interaction:

$$H_{\text{TB}} = t_1 \sum_{\langle ij \rangle \sigma} c_{i\sigma}^\dagger c_{j\sigma} + |t_2| \sum_{\langle\langle ij \rangle\rangle \sigma} e^{i\nu_{ij}\sigma\phi} c_{i\sigma}^\dagger c_{j\sigma} + U \sum_i n_{i\uparrow} n_{i\downarrow}. \quad (4)$$

Here, $\langle ij \rangle$ and $\langle\langle ij \rangle\rangle$ denote the nearest neighbor (NN) and next NN, respectively, $\nu_{ij} = +1$ (-1) if the electron makes a left (right) turn to get to the NN site, $\sigma = \pm 1$ for spin- \uparrow (spin- \downarrow) and $\phi = 2\pi/3$. Notice that the hopping parameters beyond t_2 have small but non-negligible amplitudes, we truncate the hopping terms up to t_5 while the interactions to the onsite Hubbard term. One can consult Methods or Ref. [43] for more details of the continuum model, the generation of Wannier states and the computation of the hopping and interaction parameters. **Itinerant topological magnons and spin excitons**

Now, we investigate the spin excitations out of the itinerant ferromagnetic (FM) ground state at filling $\nu = +1$, *i.e.*, one hole per moiré unit cell. Generally, the spin excitations in an itinerant system come from the electronic spin-flip particle-hole excitations. For convenience we perform a particle-hole transformation and refer a hole (an electron) as an electron (a hole). The FM ground state is expressed by $|\text{GS}\rangle = \prod_{\mathbf{k} \in 1\text{BZ}} \alpha_{\mathbf{k}l\uparrow}^\dagger |0\rangle$,

where $\alpha_{\mathbf{k}l\uparrow}^\dagger$ creates a spin- \uparrow electron on the lower band with momentum \mathbf{k} . The Hilbert space with one spin flip ($\Delta S_z = -1$) is spanned by $|\mathbf{k}, \mathbf{q}, \mu\rangle = \alpha_{\mathbf{k}+\mathbf{q}\mu\downarrow}^\dagger \alpha_{\mathbf{k}l\uparrow} |\text{GS}\rangle$, where $\mu = l(u)$ denotes the lower (upper) band. This space contains both intraband and interband spin flips, as shown in Fig. 2(a). Due to the translation symmetry, the total momentum \mathbf{q} is a good quantum number. By acting H_{TB} on the $\Delta S_z = -1$ space we obtain the Hamiltonian matrix $H(\mathbf{q})$ at each \mathbf{q} with its element $H_{\mathbf{k}\mu, \mathbf{k}'\mu'}(\mathbf{q}) = \langle \mathbf{k}, \mathbf{q}, \mu | H_{\text{TB}} | \mathbf{k}', \mathbf{q}, \mu' \rangle$. In the presence of inversion symmetry, we find $H(\mathbf{q})$ has the following compact form

$$H(\mathbf{q}) = \sum_{\mathbf{k} \mu=l,u} \left[\frac{U}{2} + \varepsilon_\mu^\dagger(\mathbf{k} + \mathbf{q}) - \varepsilon_l^\dagger(\mathbf{k}) \right] |\mathbf{k}, \mathbf{q}, \mu\rangle \langle \mathbf{k}, \mathbf{q}, \mu| - \frac{U}{N} \sum_{n=A,B} |\mathbf{q}, n\rangle \langle \mathbf{q}, n|, \quad (5)$$

where ε_μ^σ with $\mu = l(u)$ is the dispersion of the lower (upper) spin- σ electron band, $n = A, B$ denote the two sublattices of the effective honeycomb lattice, N is the number of unitcells, and $|\mathbf{q}, n\rangle \equiv \sum_{\mathbf{k}} c_{\mathbf{k}+\mathbf{q}n\downarrow}^\dagger c_{\mathbf{k}n\uparrow} |\text{GS}\rangle$. Here, $c_{\mathbf{k}n\sigma}^\dagger$ creates a spin- σ electron of sublattice n with momentum \mathbf{k} . When the inversion symmetry is explic-

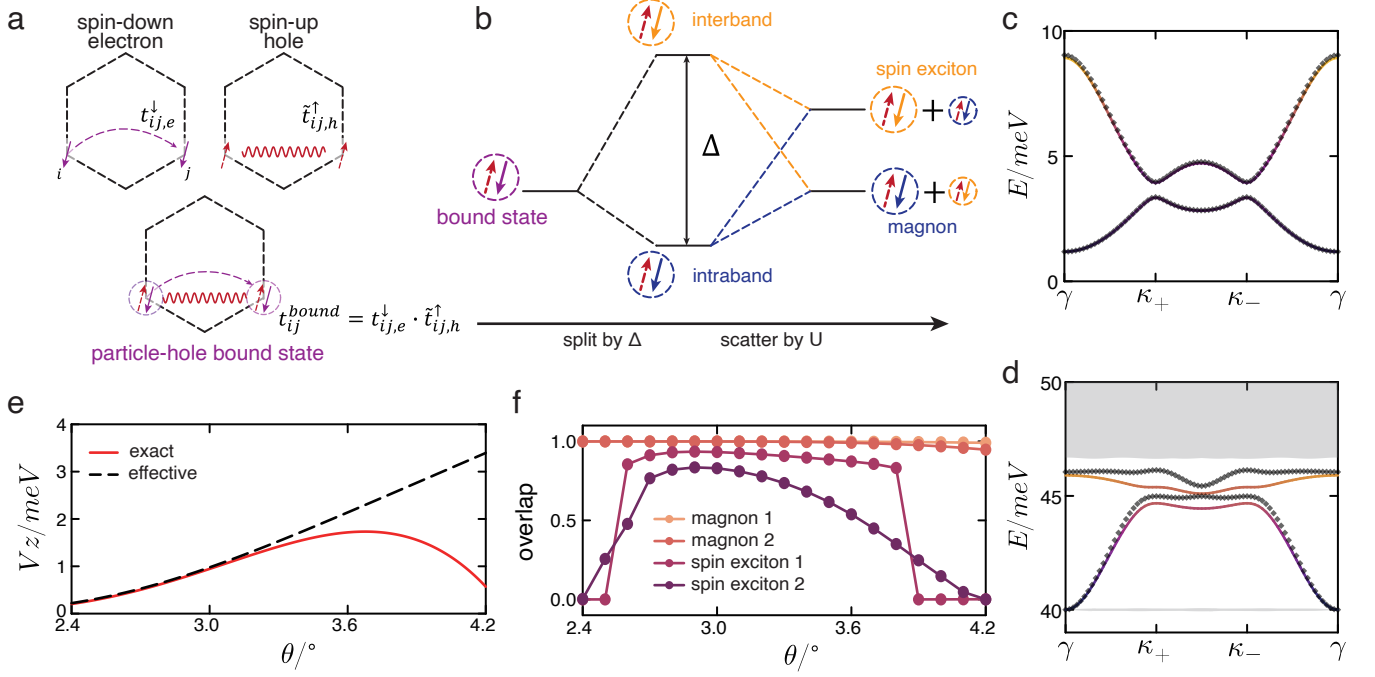


FIG. 3. **Origin of magnon and spin exciton topology.** **a**, Direct inheritance of magnon topology from electronic topology. The magnon is described as a bounded particle-hole pair in an itinerant magnetic systems, of which the hopping is the product of spin- \downarrow electron and spin- \uparrow hole, with the latter renormalized by the itinerant FM background. **b**, Magnetic effective model. The bounded particle-hole pair is splitted into its intraband and interband projections by the gap between two electron bands Δ . The two parts are further coupled by the Hubbard interaction, so that one evolves into two magnons and the other into two spin excitons. **c,d**, Comparison of the magnon (c) and spin exciton (d) dispersions derived by exact diagonalization (colored lines) and magnetic effective model (diamond lines) at $(\theta, V_z, U) = (2.94^\circ, 0, 80 \text{ meV})$. **e**, Comparison of magnon topological transition boundary. **f**, Overlap of the states derived by exact diagonalization and the magnetic effective model at κ_+ point.

itly broken by a displacement field, which equals to introducing an opposite chemical potential at different sublattices, $H(\mathbf{q})$ has a slightly more complex form, which is shown in Methods.

The spin excitations with momentum \mathbf{q} are calculated by the exact diagonalization (ED) of $H(\mathbf{q})$, which are performed on a $N = 72 \times 72$ k-mesh (such a large-scale ED calculation is possible as the $\Delta S_z = -1$ space scales linearly in N). The spectra of spin excitations along the high-symmetric direction in the moiré Brillouin zone are shown in Fig. 2(b) for 2.94° and 3.89° , which is obtained with a Hubbard interaction $U = 80 \text{ meV}$ being experimentally accessible by tuning the relative dielectric constant ε to be about 20.

Overall, the excitation spectra consist of four parts: two continua, a group of two well-defined excitations at low energies below 10 meV (2.94°) or 20 meV (3.89°), and a group of two well-defined excitations in the intermediate energies between the two continua. The differences in spectral features between the two twist angles are: 1) for a small twist angle 2.94° , the lower continuum has an almost vanishing width, 2) for a large twist angle 3.89° , both continua expand in width so that the excitations between them merge into the continua in most \mathbf{q} ranges

where the merged excitations lose the well-defined feature.

To understand the nature of these spin excitations, we resort to a qualitative analysis by inspecting each term in Eq. 5. The first term describes the scattering of the state $|\mathbf{k}, \mathbf{q}, \mu\rangle$ which involves the particle-hole excitation of a spin- \downarrow electron and a spin- \uparrow hole with the momentum $\mathbf{k} + \mathbf{q}$ and \mathbf{k} , respectively. For a fixed \mathbf{q} , the excitation band is broadened by the internal momentum \mathbf{k} into a continuum, which is exactly the Stoner continuum—a universal character of the itinerant system. Thus, from the first term of Eq. 5, we determine that the lower continuum which consists of intraband flips, locates at $U/2$ with a width of W_1 and the higher continuum which consists of interband flips, locates at $U/2 + \Delta$ with a width of $W_1 + W_2$, where Δ , $W_{1,2}$ is the average gap and widths of the two electron bands, respectively. The second term of Eq. 5, on the contrary, describes the scattering of the bound states formed by particle-hole pairs. By a Fourier transformation $|\mathbf{q}, n\rangle = \sum_i e^{i\mathbf{q}\cdot\mathbf{R}_i} c_{i\downarrow}^\dagger c_{i\uparrow} |\text{GS}\rangle$, we see that $|\mathbf{q}, n\rangle$ is a collection of the onsite spin flips $\beta_{in}^\dagger \equiv c_{i\downarrow}^\dagger c_{i\uparrow}$ projected onto the itinerant FM ground state, which is in essence the magnons and spin excitons.

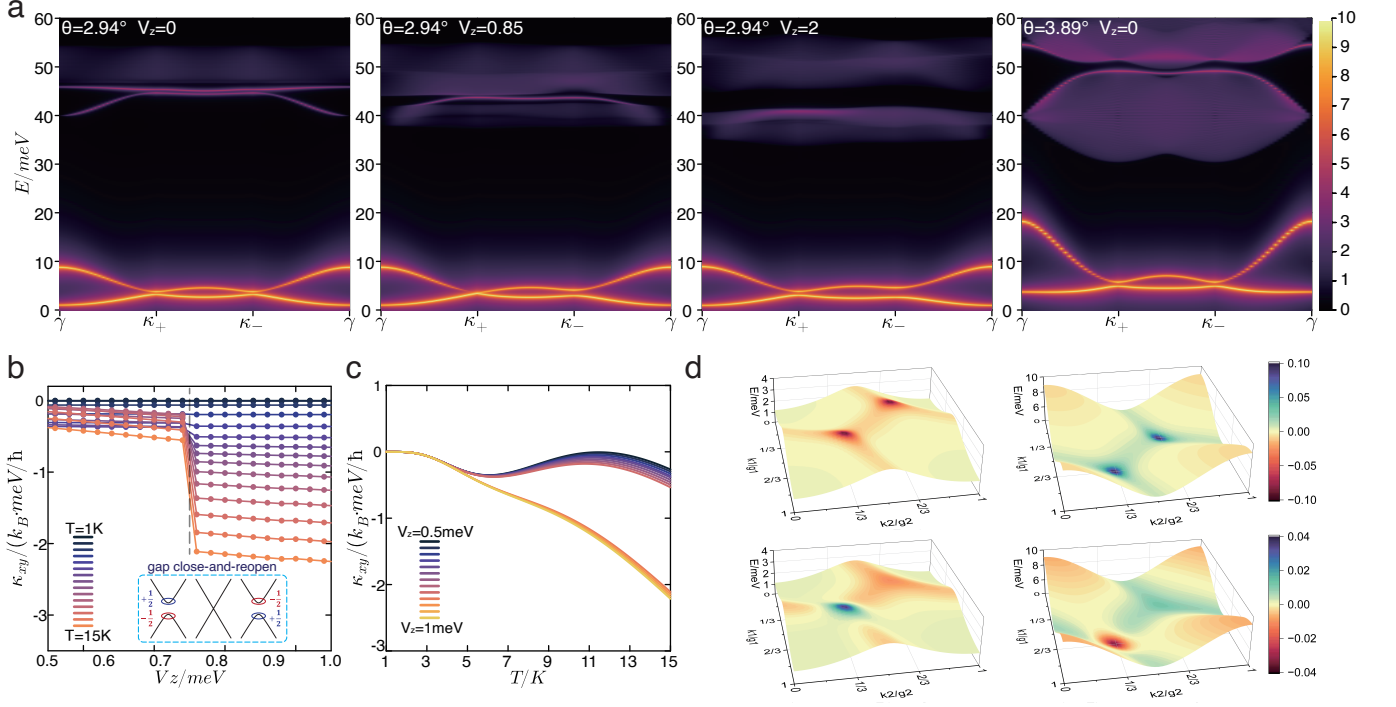


FIG. 4. **Spectral weight and thermal Hall conductance.** **a**, Logarithmic heatmap of spin structure factor. From left to right, the first three panels are calculated at $\theta = 2.94^\circ$, $V_z = (0, 0.85, 2)$ meV, $U = 80$ meV and the fourth panel at $\theta = 3.89^\circ$, $V_z = 0$, $U = 80$ meV, respectively. **b**, Thermal Hall conductance of magnons as a function of V_z . A step-like rise of thermal Hall conductance emerges at the magnon topological transition. Inset sketches the Berry curvature distribution at κ_+ right before and after the topological transition. **c**, Thermal Hall conductance of magnons as a function of T . A bifurcation appears at $\theta = 2.94^\circ$, $V_z = 0$ (top two panels) and $\theta = 2.94^\circ$, $V_z = 2$ meV (bottom two panels).

All the qualitative features based on Eq. 5 are summarized in Fig. 2(c). A comparison between Fig. 2(c) and the ED results in Fig. 2(b) confirms that the two well-defined excitations at low energies are two magnons corresponding to the acoustic and optical branches arising from the two-sublattice structure of the honeycomb lattice, two well-defined excitations at intermediate energies are two spin excitons and the others are Stoner continua. In this way, we can also understand that the lower continuum with a vanishing width at 2.94° is due to the extreme flatness of the electron band as shown in Fig. 1(d). We note that in contrast to the usual charge excitons, the identified spin excitons are lifted in energy by $U/2$ arising from the itinerant FM background.

Now, we turn to the discussion of the topological properties of itinerant magnons and spin excitons. When there is no displacement field $V_z = 0$, we find that the Chern numbers of the two gapped magnon bands are $C_m = \pm 1$, as shown in Fig. 2(d) and (e). Therefore, the itinerant magnons have nontrivial topology. Interestingly, we find that the topology of magnons can be tuned by the displacement field V_z . Increasing V_z , the gap between two magnon bands decreases, eventually closes at the κ_+ point when $V_z \approx 0.85$ meV for 2.94° and $V_z \approx 1.56$

meV for 3.89° . With a further increase of V_z , the closed gap reopens, but now the Chern numbers of both magnon bands become zero. Therefore, the tTMD not only hosts the topological itinerant magnon, but also provides an ideal way to manipulate its topological transition via the tuning of the displacement field. As for the spin exciton, we note that the high-quality flatness of the electron band, *i.e.*, the small ratio of $W_{1,2}/\Delta$, plays an essential role for the appearance of the well-defined spin excitons, as shown in Fig. 2(b). So, at a small twist angle such as $\theta = 2.94^\circ$ where the well-defined spin exciton exists, we can find that the upper spin exciton has a nonzero Chern number $C_s = +1$ for $V_z = 0$, and a transition to the topological trivial state accompanying with a gap close-and-reopen occurs as V_z increases [see Fig. 2(d)]. At a large twist angle such as 3.89° , the broadening of the topmost flat electronic bands [Fig. 1(d) and (e)] leads to a large $W_{1,2}/\Delta$, so that the spin excitons would merge into the Stoner continua and there is no possibility to consider their band topology.

In Fig. 2(f), we present a comprehensive θ - V_z phase diagram. The boundary of the metal and general FM phase is determined by the magnon instability line, which is closely related to the width of the first electron band

W_1 (see Extended Data Fig. 2). The general FM phase can be further divided into a conventional FM state (FM) with trivial electron and magnon topology, a FM state with nontrivial electron topology but trivial magnon topology resulting in a quantum anomalous Hall effect (FM+QAH), and a FM state with both nontrivial electron and magnon topology (FM+QAH+TM). It is expected that this phase diagram will stimulate and facilitate the experimental explorations of the magnetic excitations discussed in this paper.

Magnetic effective model and origin of topology

In local spin systems, the magnonic excitations are well understood as bosons in the framework of LSWT, and their nontrivial band topology is usually induced by the Dzyaloshinskii–Moriya (DM) interaction acting as the vector potential for the propagation of free magnons. However, in the case of itinerant magnets, the lack of an exact local spin per physical site, along with the absence of the corresponding effective model describing the spin wave excitations, leaves our understanding of itinerant topological spin excitations rather vague.

As shown in Fig. 2(c), the two continua and the spin excitons scale with U , while the magnons are located at rather low energies. So we first consider the simplest case focusing only on the magnons, which is equivalent to the large U limit, pushing the continua and the spin excitons to infinite energies. Given that double occupancy is excluded in this limit, we introduce a magnetic effective model consisting of the projected onsite spin flip operators $\tilde{\beta}_{in}^\dagger \equiv \beta_{in}^\dagger |\text{GS}\rangle \langle \text{GS}|$, based on an analogy with the LSWT where the local spin flip is mapped into a hardcore boson,

$$H_{\text{mag}} = \sum_{ij} t_{ij}^{\text{bound}} \tilde{\beta}_i^\dagger \tilde{\beta}_j \quad (6)$$

where the sublattice index is absorbed into the site index, $t_{ij}^{\text{bound}} \equiv \langle \text{GS} | \beta_i H_{\text{TB}} \beta_j^\dagger | \text{GS} \rangle$ is the hopping of the projected onsite spin flip, which corresponds to the hopping of a magnon in the itinerant FM system. In fact, the extraction of the magnetic effective model equals to reducing the $\Delta S_z = -1$ space to $B_2 \equiv \{|\mathbf{q}, A\rangle, |\mathbf{q}, B\rangle\}$ and the Hamiltonian $H(\mathbf{q})$ to a 2×2 matrix with its element $H_{mn}(\mathbf{q}) = \langle \mathbf{q}, m | H_{\text{TB}} | \mathbf{q}, n \rangle$, with $m, n = A, B$. By diagonalizing the reduced Hamiltonian matrix, we perfectly reproduce the magnon dispersion (see Extended Data Fig. 3), which confirms the fact that the nature of the itinerant magnon is the onsite spin flip β_{in}^\dagger projected onto the itinerant FM ground state. As sketched in Fig. 3(a), t_{ij}^{bound} can be directly expressed as the product of the hopping of a spin- \downarrow electron $t_{ij,e}^\downarrow$ and an effective hopping of a spin- \uparrow hole $t_{ij,h}^\uparrow$ (proof can be found in Methods), so the nonzero phase factor of the next NN hopping of electrons would enter into that of magnons. The magnetic effective model thus resembles a bosonic version of the Haldane model [52] which has staggered flux (com-

plex t_2^{bound}) while the net flux is zero (real t_1^{bound}). It demonstrates unambiguously that the topology of itinerant magnons inherits directly from the topology of electrons.

We point out that the origin of the magnon topology in itinerant systems is essentially different from that in local spin systems. The former is induced by a direct electron hopping depending on t but irrelevant to U , while the latter comes from the effective spin-spin interaction, *e.g.*, the DM interaction, which is a second-order virtual process depending on t^2/U . We also note that the effective $t_{ij,h}^\uparrow$ stems from the charge fluctuations of the FM ground state (see Methods), which is only nonzero in itinerant systems but vanishes in local spin systems.

In the realistic circumstance in this paper where U is finite (equal to 80 meV) and the electronic energy gap Δ not too small (about 10meV), we can include the spin excitons in our magnetic effective model by considering the effect of Δ . As depicted in Fig. 3(b), Δ splits the bound states into the intraband and interband projections. Concurrently, a finite U couples these two parts, resulting in the formation of low-energy magnons (primarily the intraband part with a minor interband contribution) and high-energy spin excitons (primarily the interband part with a minor intraband contribution), both of which are bound states. This partitioning of magnons and spin excitons aligns with the exact results presented in Fig. 2. In order to account for all these physical processes, it is necessary to construct a magnetic effective model based on the enlarged bases $B_4 \equiv \{P_l |\mathbf{q}, A\rangle, P_u |\mathbf{q}, A\rangle, P_l |\mathbf{q}, B\rangle, P_u |\mathbf{q}, B\rangle\}$, which are composed of the split bound states $P_{l,u} \beta_{in}^\dagger |\text{GS}\rangle$. Here, P_l (P_u) is the projection operator onto the lower (upper) electron band. In this way, one can quantitatively check the effectiveness of the magnetic effective model and physical picture sketched in Fig. 3(b). By diagonalizing the 4×4 Hamiltonian matrix constructed in the B_4 space, we can obtain the eigenvalues $E_{\mathbf{q}}$ and eigenstates $\phi_i(\mathbf{q})$. In Fig. 3(c)-(d) and Fig. 3(e), we present the obtained results for the spin excitation spectra $E_{\mathbf{q}}$ and the boundary of the topological transition of magnons, respectively, along with those calculated from ED as colored lines. In Fig. 3(f), the overlap $P_n(\mathbf{q}) \equiv \sum_i |\langle \psi_n(\mathbf{q}) | \phi_i(\mathbf{q}) \rangle|^2$ of the eigenstates are shown, where $\psi_n(\mathbf{q})$ are those obtained by the ED calculation. An overall comparison shows clearly that in the range of the twisted angles $2.7^\circ \sim 3.3^\circ$, the description of the magnons based on the magnetic effective model coincides perfectly with the ED calculation, and the overlap of the spin excitons between the two methods is over 0.75. It confirms that the physical picture for the magnon and spin exciton based on the magnetic effective model [Fig. 3(b)] is reasonable. Based on this picture, one can see that the spin excitons evolve from the projected onsite spin-flip states, which acquire a nonzero phase factor in their NN hopping inheriting from that in

the electron hoppings. Therefore, the topology of spin excitons also stems from the topology of electrons.

Dynamical Spin structure factor

We have established that topological magnons and spin excitons exist in tTMD with an itinerant FM ground state in a wide range of small twist angles and a transition to trivial excitations can be tuned by adjusting the displacement field. Considering that the tuning of the displacement field is the popular and unique way in tTMD to adjust continuously the electronic structure, the tTMD provides a competitive system to probe the topological properties of these spin excitations.

The first experimental observable is the dynamical spin structure factor, which reflects both the dispersion and the spectral weight of the excitations. Via the definition of the bosonic spin operator $\beta_{\mathbf{q}n}^\dagger$, we can calculate the spin structure factor $-\frac{1}{\pi}\text{Im}G^R(\mathbf{k}, \omega)$ via the retarded Green's function $G^R(\mathbf{k}, \omega)$ given by,

$$G^R(\mathbf{q}, \omega) = \sum_{mn} \frac{|\langle \psi_m(\mathbf{q}) | \beta_{\mathbf{q}n}^\dagger | \text{GS} \rangle|^2}{\omega - \omega_{m\mathbf{q}} + i\delta} \quad (7)$$

where m sums over all the eigenstates $|\psi_m(\mathbf{q})\rangle$ with total momentum \mathbf{q} in $\Delta S_z = -1$ space and $\omega_{m\mathbf{q}}$ is the corresponding eigen energy, $n = A, B$ the sublattice index, $\beta_{\mathbf{q}n}^\dagger$ the Fourier transformation of β_{in}^\dagger . The results for two twisted angle 2.94° and 3.89° are shown in Fig. 4(a). Overall, most spectral weights concentrate on the magnons and spin excitons, especially the two magnon bands. So, it will facilitate the probe of these two bound states. For the small twisted angle 2.94° and $V_z = 0$, where the topmost electron band becomes nearly complete flat, the lower Stoner continuum almost does not show up and the upper one also has a weak spectra weight. For the large twisted angle 3.89° , where the topmost electron band becomes much more dispersive, the two Stoner continua acquire more weight. In this case, the obvious bright edges of Stoner continua in fact reflect the weight of the spin excitons, but it is difficulty to distinguish them from the continua. So, the test of the topological magnon and spin exciton experimentally is more suitable around the magic angle 2.94° . We note that, with the increase of V_z , a linear Dirac dispersion of the magnon bands emerges at κ_+ point when the gap between two magnons vanishes, *i.e.*, at the magnon topological transition, which can be probed by a spectral weight detection.

Thermal Hall conductance

In recent years, the thermal Hall conductivity has emerged as a practical and insightful physical quantity for detecting topological states and characterizing the topological phase transitions in magnetic systems. In this regard, we will study the thermal Hall conductance of the topological spin excitations and its variation with the displacement field. As discussed above, the spin exciton is in fact fragile to the changes of displacement

fields and it also situates in a high-energy region which has negligible effect for the thermal Hall conductance at low temperatures we considered, so we only focus on the contribution of magnons. The thermal Hall conductance κ_{xy}^m of magnons can be calculated by use of the linear response theory [53] as following,

$$\kappa_{xy}^m = -\frac{k_B^2 T}{\hbar} \sum_{n\mathbf{k}} \left(c_2 [g(\varepsilon_{n\mathbf{k}})] - \frac{\pi^2}{3} \right) \Omega_{n\mathbf{k}}. \quad (8)$$

Where the band index n sums over the two magnon bands, $g(\varepsilon)$ is the Bose-Einstein distribution function and $c_2(x) = \int_0^x dt (\ln \frac{1+t}{t})^2$, and $\Omega_{n\mathbf{k}}$ the Berry curvature of the n magnon bands at momentum \mathbf{k} . In Fig. 4(b), we show κ_{xy}^m as a function of V_z for different temperature T . Firstly, we need to point out that there is no quantized behavior of κ_{xy}^m as that of electron, due to the bosonic character of the spin excitation. Starting from the lowest temperature $T = 1\text{K}$, one can see that there is essentially no thermal Hall conductance in the whole V_z range up to 1.0 meV, though the magnons are topologically nontrivial for V_z below 1.0 meV. With the gradual increase of T , a noticeable finite κ_{xy}^m appears and grows with V_z , but it always exhibits flat κ_{xy}^m with V_z until $T = 5\text{K}$. When $T > 5\text{K}$, a step-like increase in the magnitude of κ_{xy}^m occurs at the topological transition point where the gap between two magnons closes and reopens. The same phenomenon manifests itself in the temperature dependence of κ_{xy}^m as shown in Fig. 4(c). The thermal Hall conductance shows stark distinct T -dependence before and after topological transition via the tuning of the displacement field V_z and exhibits an obvious bifurcation. We propose that these two remarkable dependences of κ_{xy}^m on V_z and T , as a compelling evidence on the topological transition we proposed here, can be used as an experimental test.

To explore the physical reason of these phenomena, we note that the essential factor determining the behavior of the thermal Hall conductance is the distribution of the Berry curvature in the momentum space, which plays a similar role to the density of states in the usual electron conductivity. Hence, we show the calculated results of $\Omega_{n\mathbf{k}}$ in Fig. 4(d) for the two magnons at $\theta = 2.94^\circ$ with $V_z = 0$ and $V_z = 2$ meV, respectively. It shows that the magnitude of $\Omega_{n\mathbf{k}}$ increases gradually from γ point to κ_+ and κ_- points, and forms two peaks around κ_+ and κ_- . For $V_z = 0$, $\Omega_{n\mathbf{k}}$ has the same sign for the acoustic and optical magnons and the same magnitude at κ_+ and κ_- points. On the other hand, for $V_z = 2$ meV where the two reopened magnon bands have zero Chern number, each of the two magnons exhibits opposite $\Omega_{n\mathbf{k}}$ in the momentum space. This explains why the magnon bands have nonzero Chern number at $V_z = 0$ and zero Chern number at $V_z = 2$ meV, as the total contribution of the Berry curvature to the Chern number cancels out in the latter case. Having the knowledge of the Berry curvature, we are now at the position to understand the phenomena

shown in Fig. 4(b) and (c). At low temperatures, only the low-energy magnons around γ can be thermally excited, they have tiny contribution to the thermal Hall conductance. With the increase of temperature, those magnons near the κ_+ and κ_- points carrying the majority of Berry curvature are involved gradually. The step-like rise in κ_{xy}^m across the topological transition can be attributed to the quantized change of the Berry curvature from $\mp 1/2$ to $\pm 1/2$ at κ_+ , where the gap closes and reopens, as shown in the inset of Fig. 4(b). Due to the bosonic character of the magnon characterized in the prefactor $c_2[g(\epsilon)]$, the magnitude of the step-like rise depends on temperature. In the case of 3.89° (see Extended Data Fig. 4), accompanying the similar step-like change across the transition, a sign reversal of thermal Hall conductance also emerges, which is due to the detail distribution of the Berry curvature in the momentum space. Due to the same physical reason, the temperature dependence of thermal Hall conductance also exhibits noticeable bifurcation when the displacement field V_z crosses the transition point.

Finally, we note that as an itinerant FM system, the total thermal Hall conductance includes both contributions of magnon and electron bands. However, it is expected that the step-like and bifurcation features unveiled above would not be blurred by the electronic contributions κ_{xy}^e . First, the phase diagram Fig. 2(f) tells us that the magnon topological transition occurs at a far smaller V_z than that of electron (about 7 meV at 2.94°). The Berry curvature of electron bands changes little at that small V_z , so does κ_{xy}^e . Second, as κ_{xy}^e is proportional to the electron Hall conductance σ_{xy}^e to a temperature dependent factor, one can filter out κ_{xy}^e from the total κ_{xy} by detecting σ_{xy}^e .

Summary and discussion

In summary, we theoretically predict the existence of itinerant topological magnons and spin excitons in a large range of twisted angles in tMoTe₂. We demonstrate that the topology of the itinerant magnons and spin excitons can be tuned by displacement field V_z , and the topological transition can be experimentally identified by a step-like rise in the V_z dependence and a bifurcation in the temperature dependence of thermal Hall conductance. We elaborate that the topology of itinerant magnons and spin excitons originates directly from that of electrons, in that the hopping of magnons and spin excitons as particle-hole bound states, acquires a flux from that of the underlying electrons. This mechanism differs from that in local spin systems, where the topological magnons are typically induced by the Dzyaloshinskii–Moriya interaction.

Our work has raised the following prospects. First, as discussed above, itinerant topological magnons and spin excitons naturally emerge above the ferromagnetic ground state within a topological electronic flat band, a scenario that is quite common in tTMDs. This is attributed to the high tunability of tTMDs in terms of

bandwidth and electron filling, which enables the observation of these exotic excitations in various tTMD materials across a wide range of twist angles. Second, the magnetic effective model describing itinerant magnons as particle-hole bound states, can serve as a good starting point to theoretically investigate the spin excitations in itinerant FM systems, which may not be restricted to integer filling per unit cell. In the flat-band limit, we can easily inspect the evolution of itinerant magnons by continuously varying the filling factor, assuming an appropriate itinerant FM ground state. Finally, we propose that the exotic spin excitations and topological transition could be probed by spectral measurements and heat transport experiments, which are still rare in the investigation of tTMDs. We believe that the theoretical predictions presented here can inspire further advancements in such experiments in tTMDs. Our work deepens the understanding of spin excitations in itinerant electron systems with flat bands and paves the way for future experiments investigating spintronics in tTMDs.

Note added.— After completing this work, we learned that a related study by W.-X. Qiu *et al.* also find theoretically the topological magnons in tMoTe₂.

* These authors contributed equally to the work.

† waltergu@nju.edu.cn

‡ jxli@nju.edu.cn

- [1] E. C. Regan, D. Wang, C. Jin, M. I. B. Utama, B. Gao, X. Wei, S. Zhao, W. Zhao, Z. Zhang, K. Yumigeta, M. Blei, J. D. Carlström, K. Watanabe, T. Taniguchi, S. Tongay, M. Crommie, A. Zettl, and F. Wang, Mott and generalized wigner crystal states in wse2/ws2 moiré superlattices, *Nature* **579**, 359 (2020).
- [2] T. Li, S. Jiang, L. Li, Y. Zhang, K. Kang, J. Zhu, K. Watanabe, T. Taniguchi, D. Chowdhury, L. Fu, J. Shan, and K. F. Mak, Continuous mott transition in semiconductor moiré superlattices, *Nature* **597**, 350 (2021).
- [3] E. C. Regan, Z. Lu, D. Wang, Y. Zhang, T. Devakul, J. H. Nie, Z. Zhang, W. Zhao, K. Watanabe, T. Taniguchi, S. Tongay, A. Zettl, L. Fu, and F. Wang, Spin transport of a doped mott insulator in moiré heterostructures, *Nature Communications* **15**, 10252 (2024).
- [4] Y. Xu, S. Liu, D. A. Rhodes, K. Watanabe, T. Taniguchi, J. Hone, V. Elser, K. F. Mak, and J. Shan, Correlated insulating states at fractional fillings of moiré superlattices, *Nature* **587**, 214 (2020).
- [5] H. Li, S. Li, E. C. Regan, D. Wang, W. Zhao, S. Kahn, K. Yumigeta, M. Blei, T. Taniguchi, K. Watanabe, S. Tongay, A. Zettl, M. F. Crommie, and F. Wang, Imaging two-dimensional generalized wigner crystals, *Nature* **597**, 650 (2021).
- [6] H. Li, Z. Xiang, A. P. Reddy, T. Devakul, R. Sailus, R. Banerjee, T. Taniguchi, K. Watanabe, S. Tongay, A. Zettl, L. Fu, M. F. Crommie, and F. Wang, Wigner molecular crystals from multielectron moiré artificial atoms, *Science* **385**, 86 (2024).

- [7] Y. Xia, Z. Han, K. Watanabe, T. Taniguchi, J. Shan, and K. F. Mak, Superconductivity in twisted bilayer wse₂, *Nature* **637**, 833 (2025).
- [8] Y. Guo, J. Pack, J. Swann, L. Holtzman, M. Cothrine, K. Watanabe, T. Taniguchi, D. G. Mandrus, K. Barmak, J. Hone, A. J. Millis, A. Pasupathy, and C. R. Dean, Superconductivity in 5.0° twisted bilayer wse₂, *Nature* **637**, 839 (2025).
- [9] W. Zhao, B. Shen, Z. Tao, Z. Han, K. Kang, K. Watanabe, T. Taniguchi, K. F. Mak, and J. Shan, Gate-tunable heavy fermions in a moiré kondo lattice, *Nature* **616**, 61 (2023).
- [10] D. Guerci, J. Wang, J. Zang, J. Cano, J. H. Pixley, and A. Millis, Chiral kondo lattice in doped mote₂/wse₂ bilayers, *Science Advances* **9**, eade7701 (2023), <https://www.science.org/doi/pdf/10.1126/sciadv.ade7701>.
- [11] L. Wang, E.-M. Shih, A. Ghiotto, L. Xian, D. A. Rhodes, C. Tan, M. Claassen, D. M. Kennes, Y. Bai, B. Kim, K. Watanabe, T. Taniguchi, X. Zhu, J. Hone, A. Rubio, A. N. Pasupathy, and C. R. Dean, Correlated electronic phases in twisted bilayer transition metal dichalcogenides, *Nature Materials* **19**, 861 (2020).
- [12] Y. Tang, L. Li, T. Li, Y. Xu, S. Liu, K. Barmak, K. Watanabe, T. Taniguchi, A. H. MacDonald, J. Shan, and K. F. Mak, Simulation of hubbard model physics in wse₂/ws₂ moiré superlattices, *Nature* **579**, 353 (2020).
- [13] P. Merkl, F. Mooshammer, S. Brem, A. Girnghuber, K.-Q. Lin, L. Weigl, M. Liebich, C.-K. Yong, R. Gillen, J. Maultzsch, J. M. Lupton, E. Malic, and R. Huber, Twist-tailoring coulomb correlations in van der waals homobilayers, *Nature Communications* **11**, 2167 (2020).
- [14] X. Huang, T. Wang, S. Miao, C. Wang, Z. Li, Z. Lian, T. Taniguchi, K. Watanabe, S. Okamoto, D. Xiao, S.-F. Shi, and Y.-T. Cui, Correlated insulating states at fractional fillings of the ws₂/wse₂ moiré lattice, *Nature Physics* **17**, 715 (2021).
- [15] J. Gu, L. Ma, S. Liu, K. Watanabe, T. Taniguchi, J. C. Hone, J. Shan, and K. F. Mak, Dipolar excitonic insulator in a moiré lattice, *Nature Physics* **18**, 395 (2022).
- [16] E. Anderson, F.-R. Fan, J. Cai, W. Holtzmann, T. Taniguchi, K. Watanabe, D. Xiao, W. Yao, and X. Xu, Programming correlated magnetic states with gate-controlled moiré geometry, *Science* **381**, 325 (2023), <https://www.science.org/doi/pdf/10.1126/science.adg4268>.
- [17] W. Zhao, K. Kang, Y. Zhang, P. Knüppel, Z. Tao, L. Li, C. L. Tschirhart, E. Redekop, K. Watanabe, T. Taniguchi, A. F. Young, J. Shan, and K. F. Mak, Realization of the haldane chern insulator in a moiré lattice, *Nature Physics* **20**, 275 (2024).
- [18] K. Kang, B. Shen, Y. Qiu, Y. Zeng, Z. Xia, K. Watanabe, T. Taniguchi, J. Shan, and K. F. Mak, Evidence of the fractional quantum spin hall effect in moiré mote₂, *Nature* **628**, 522 (2024).
- [19] T. Li, S. Jiang, B. Shen, Y. Zhang, L. Li, Z. Tao, T. Devakul, K. Watanabe, T. Taniguchi, L. Fu, J. Shan, and K. F. Mak, Quantum anomalous hall effect from intertwined moiré bands, *Nature* **600**, 641 (2021).
- [20] J. Cai, E. Anderson, C. Wang, X. Zhang, X. Liu, W. Holtzmann, Y. Zhang, F. Fan, T. Taniguchi, K. Watanabe, Y. Ran, T. Cao, L. Fu, D. Xiao, W. Yao, and X. Xu, Signatures of fractional quantum anomalous hall states in twisted mote₂, *Nature* **622**, 63 (2023).
- [21] H. Park, J. Cai, E. Anderson, Y. Zhang, J. Zhu, X. Liu, C. Wang, W. Holtzmann, C. Hu, Z. Liu, T. Taniguchi, K. Watanabe, J.-H. Chu, T. Cao, L. Fu, W. Yao, C.-Z. Chang, D. Cobden, D. Xiao, and X. Xu, Observation of fractionally quantized anomalous hall effect, *Nature* **622**, 74 (2023).
- [22] F. Xu, Z. Sun, T. Jia, C. Liu, C. Xu, C. Li, Y. Gu, K. Watanabe, T. Taniguchi, B. Tong, J. Jia, Z. Shi, S. Jiang, Y. Zhang, X. Liu, and T. Li, Observation of integer and fractional quantum anomalous hall effects in twisted bilayer mote₂, *Phys. Rev. X* **13**, 031037 (2023).
- [23] Y. Zeng, Z. Xia, K. Kang, J. Zhu, P. Knüppel, C. Vaswani, K. Watanabe, T. Taniguchi, K. F. Mak, and J. Shan, Thermodynamic evidence of fractional chern insulator in moiré mote₂, *Nature* **622**, 69 (2023).
- [24] B. A. Foutty, C. R. Kometter, T. Devakul, A. P. Reddy, K. Watanabe, T. Taniguchi, L. Fu, and B. E. Feldman, Mapping twist-tuned multiband topology in bilayer wse₂, *Science* **384**, 343 (2024).
- [25] L. Zhang, J. Ren, J.-S. Wang, and B. Li, Topological magnon insulator in insulating ferromagnet, *Phys. Rev. B* **87**, 144101 (2013).
- [26] A. Mook, J. Henk, and I. Mertig, Magnon hall effect and topology in kagome lattices: A theoretical investigation, *Phys. Rev. B* **89**, 134409 (2014).
- [27] A. Mook, J. Henk, and I. Mertig, Edge states in topological magnon insulators, *Phys. Rev. B* **90**, 024412 (2014).
- [28] S. A. Owerre, A first theoretical realization of honeycomb topological magnon insulator, *Journal of Physics: Condensed Matter* **28**, 386001 (2016).
- [29] P. Laurell and G. A. Fiete, Magnon thermal hall effect in kagome antiferromagnets with dzyaloshinskii-moriya interactions, *Phys. Rev. B* **98**, 094419 (2018).
- [30] R. Seshadri and D. Sen, Topological magnons in a kagome-lattice spin system with *xxz* and dzyaloshinskii-moriya interactions, *Phys. Rev. B* **97**, 134411 (2018).
- [31] S. A. Díaz, J. Klinovaja, and D. Loss, Topological magnons and edge states in antiferromagnetic skyrmion crystals, *Phys. Rev. Lett.* **122**, 187203 (2019).
- [32] Y.-S. Lu, J.-L. Li, and C.-T. Wu, Topological phase transitions of dirac magnons in honeycomb ferromagnets, *Phys. Rev. Lett.* **127**, 217202 (2021).
- [33] P. A. McClarty, Topological magnons: A review, *Annual Review of Condensed Matter Physics* **13**, 171 (2022).
- [34] M. dos Santos Dias, N. Biniskos, F. J. dos Santos, K. Schmalzl, J. Persson, F. Bourdarot, N. Marzari, S. Blügel, T. Brückel, and S. Lounis, Topological magnons driven by the dzyaloshinskii-moriya interaction in the centrosymmetric ferromagnet mn₅ge₃, *Nature Communications* **14**, 7321 (2023).
- [35] H. Tasaki, Ferromagnetism in the hubbard models with degenerate single-electron ground states, *Phys. Rev. Lett.* **69**, 1608 (1992).
- [36] H. Tasaki, From nagaoka's ferromagnetism to flat-band ferromagnetism and beyond: An introduction to ferromagnetism in the hubbard model, *Progress of Theoretical Physics* **99**, 489 (1998).
- [37] X.-F. Su, Z.-L. Gu, Z.-Y. Dong, and J.-X. Li, Topological magnons in a one-dimensional itinerant flatband ferromagnet, *Phys. Rev. B* **97**, 245111 (2018).
- [38] X.-F. Su, Z.-L. Gu, Z.-Y. Dong, S.-L. Yu, and J.-X. Li, Ferromagnetism and spin excitations in topological hubbard models with a flat band, *Phys. Rev. B* **99**, 014407 (2019).
- [39] Z.-L. Gu, Z.-Y. Dong, S.-L. Yu, and J.-X. Li, Itinerant topological magnons in haldane hubbard model with a

- nearly-flat electron band (2019), arXiv:1908.09255 [cond-mat.str-el].
- [40] Z.-L. Gu and J.-X. Li, Itinerant topological magnons in $su(2)$ symmetric topological hubbard models with nearly flat electronic bands, Chinese Physics Letters **38**, 057501 (2021).
- [41] F. Wu, T. Lovorn, E. Tutuc, I. Martin, and A. H. MacDonald, Topological insulators in twisted transition metal dichalcogenide homobilayers, Phys. Rev. Lett. **122**, 086402 (2019).
- [42] H. Pan, F. Wu, and S. Das Sarma, Band topology, hubbard model, heisenberg model, and dzyaloshinskii-moriya interaction in twisted bilayer wse_2 , Phys. Rev. Res. **2**, 033087 (2020).
- [43] T. Devakul, V. Crépel, Y. Zhang, and L. Fu, Magic in twisted transition metal dichalcogenide bilayers, Nature Communications **12**, 6730 (2021).
- [44] C. Wang, X.-W. Zhang, X. Liu, Y. He, X. Xu, Y. Ran, T. Cao, and D. Xiao, Fractional chern insulator in twisted bilayer $mote_2$, Phys. Rev. Lett. **132**, 036501 (2024).
- [45] N. Morales-Durán, N. Wei, J. Shi, and A. H. MacDonald, Magic angles and fractional chern insulators in twisted homobilayer transition metal dichalcogenides, Phys. Rev. Lett. **132**, 096602 (2024).
- [46] R. Bistritzer and A. H. MacDonald, Moiré bands in twisted double-layer graphene, Proceedings of the National Academy of Sciences **108**, 12233 (2011).
- [47] J. M. B. Lopes dos Santos, N. M. R. Peres, and A. H. Castro Neto, Continuum model of the twisted graphene bilayer, Phys. Rev. B **86**, 155449 (2012).
- [48] G. Tarnopolsky, A. J. Kruchkov, and A. Vishwanath, Origin of magic angles in twisted bilayer graphene, Phys. Rev. Lett. **122**, 106405 (2019).
- [49] Z. Song, Z. Wang, W. Shi, G. Li, C. Fang, and B. A. Bernevig, All magic angles in twisted bilayer graphene are topological, Phys. Rev. Lett. **123**, 036401 (2019).
- [50] C. L. Kane and E. J. Mele, Quantum spin hall effect in graphene, Phys. Rev. Lett. **95**, 226801 (2005).
- [51] C. L. Kane and E. J. Mele, Z_2 topological order and the quantum spin hall effect, Phys. Rev. Lett. **95**, 146802 (2005).
- [52] F. D. M. Haldane, Model for a quantum hall effect without landau levels: Condensed-matter realization of the "parity anomaly", Phys. Rev. Lett. **61**, 2015 (1988).
- [53] R. Matsumoto, R. Shindou, and S. Murakami, Thermal hall effect of magnons in magnets with dipolar interaction, Phys. Rev. B **89**, 054420 (2014).

ACKNOWLEDGMENTS

The work was supported by National Key Projects for Research and Development of China (Grant No. 2021YFA1400400), the National Natural Science Foundation of China (Grant No. 92165205, No. 12434005 and No. 12404174), and Natural Science Foundation of Jiangsu province (Grant No. BK20230765). We thank e-Science Center of Collaborative Innovation Center of Advanced Microstructures for support in allocation of CPU.

AUTHOR CONTRIBUTIONS

Z.-L.G. and J.-X.L. conceived the project. W.-T.Z. carried out the numerical calculations with the help of Z.-Y.D. and Z.-L.G. W.-T.Z., Z.-Y.D., Z.-L.G. and J.-X.L. performed the theoretical analyses and wrote the manuscript. J.-X.L. supervised the work.

COMPETING INTEREST DECLARATION

The authors declare no competing interest.

DATA AVAILABILITY

The data that support the findings of this study are available from the corresponding authors upon request.

Supplemental material for "Itinerant topological magnons and spin excitons in twisted transition metal dichalcogenides: Mapping electron topology to spin counterpart"

Wei-Tao Zhou,^{1,*} Zhao-Yang Dong,^{2,*} Zhao-Long Gu,^{1,3,†} and Jian-Xin Li^{1,3,‡}

¹National Laboratory of Solid State Microstructures and Department of Physics, Nanjing University, 210093 Nanjing, China

²Department of Applied Physics, Nanjing University of Science and Technology, Nanjing 210094, China

³Collaborative Innovation Center of Advanced Microstructures, Nanjing University, 210093 Nanjing, China

(Dated: February 18, 2025)

METHODS

Tight-binding model

To generate a tight-binding model and the corresponding Wannier basis in the subspace of our interest is to fix a gauge freedom at each momentum \mathbf{k} , which is a $U(1)$ phase for subspace containing only one band, a $U(1) \times SU(2)$ matrix for two bands and a $U(1) \times SU(N)$ matrix for N bands. In order for the tight-binding model to be a good one, the Wannier basis should be as localized as possible so that the hopping would fast vanish with the distance to present a compact tight-binding Hamiltonian by proper cut off (see Extended Data Fig. 5).

From continuum model the eigen state $\psi_{\mu\mathbf{k}}(\mathbf{r})$ has the following form

$$\psi_{\mu\mathbf{k}}(\mathbf{r}) = \sum_{\mathbf{G}} \sum_{l=b,t} a_{\mu\mathbf{k}l}^{\mathbf{G}} \chi_{\mathbf{k}l}^{\mathbf{G}}(\mathbf{r}) \quad (1)$$

where μ, l is the band and layer index, respectively. $\mathbf{G} = n_1\mathbf{g}_1 + n_2\mathbf{g}_2$, $\mathbf{g}_{1,2}$ is the reciprocal wave vector. \mathbf{G} sums over reciprocal lattice sites in the cut off $|\mathbf{G}| \leq t|\mathbf{g}_1|$ ($t = 3$ is often enough for convergence). In the plane-wave approximation, $\chi_{\mathbf{k}l}^{\mathbf{G}}(\mathbf{r}) = \eta_l e^{i(\mathbf{k}+\mathbf{G})\cdot\mathbf{r}}$ and $\eta_l = (1, 0)^T$ or $(0, 1)^T$ for bottom/top layer.

Instead of strictly obeying the maximally localized Wannier function criterion, we generate the Wannier states from a semiclassical point of view. As shown in Fig.5(b), $\Delta_{b,t}(\mathbf{r})$ reaches its maximum at XM/MX stacking region which serves as a quantum well to confine the electron. We can first perform a layer polarization $\varphi'_{n\mathbf{k}}(\mathbf{r}) = \psi_{\mu\mathbf{k}}(\mathbf{r})U_{\mu n}^{\dagger}(\mathbf{k})$ to maximize $\langle \varphi'_{1\mathbf{k}} | P_b | \varphi'_{1\mathbf{k}} \rangle$ and $\langle \varphi'_{2\mathbf{k}} | P_t | \varphi'_{2\mathbf{k}} \rangle$, $U'(\mathbf{k})$ is an $SU(2)$ matrix, $P_{b,t}$ is the projection to the bottom/top layer acting on η_l

$$P_b = \begin{pmatrix} 1 & 0 \\ 0 & 0 \end{pmatrix}, P_t = \begin{pmatrix} 0 & 0 \\ 0 & 1 \end{pmatrix} \quad (2)$$

There remains a $U(1)$ gauge freedom $\varphi'_{n\mathbf{k}}(\mathbf{r}) \rightarrow \varphi_{n\mathbf{k}}(\mathbf{r}) = \varphi'_{n\mathbf{k}}(\mathbf{r})e^{i\phi_{n\mathbf{k}}}$ for each $\varphi'_{n\mathbf{k}}(\mathbf{r})$. We fix this $U(1)$ phase so that for each momentum \mathbf{k} , $\varphi_{1\mathbf{k}}(\mathbf{r}_{\text{XM}})$ and $\varphi_{2\mathbf{k}}(\mathbf{r}_{\text{MX}})$ are real and positive, that is, the Wannier states $W_n(\mathbf{r}) = N^{-1/2} \sum_{\mathbf{k}} \varphi_{n\mathbf{k}}(\mathbf{r})$ would concentrate on the XM stacking region in the bottom layer for $n = 1$ and on the MX stacking region in the top layer for $n = 2$. Finally, we obtain the Wannier states whose Fourier transformation is $\varphi_{n\mathbf{k}}(\mathbf{r}) = \sum_{\mu} \psi_{\mu\mathbf{k}}(\mathbf{r})U_{\mu n}^{\dagger}(\mathbf{k})$ and $U^{\dagger}(\mathbf{k})$ takes the form

$$U^{\dagger}(\mathbf{k}) = U'^{\dagger}(\mathbf{k}) \begin{pmatrix} e^{i\phi_{1\mathbf{k}}} & 0 \\ 0 & e^{i\phi_{2\mathbf{k}}} \end{pmatrix} \quad (3)$$

The hopping parameters and interaction strengths can be directly calculated by

$$t_{im,jn}^{\sigma} = \int d\mathbf{r} W_m^{\sigma*}(\mathbf{r} - \mathbf{R}_i) H(\mathbf{r}) W_n^{\sigma}(\mathbf{r} - \mathbf{R}_j) \quad (4)$$

$$U_{im,jn} = \int d\mathbf{r}_1 d\mathbf{r}_2 |W_{m\mathbf{R}_i}(\mathbf{r}_1)|^2 V(|\mathbf{r}_1 - \mathbf{r}_2|) |W_{n\mathbf{R}_j}(\mathbf{r}_2)|^2 \quad (5)$$

where $V(\mathbf{r})$ is a gate-screened Coulomb interaction, its Fourier transform $V(\mathbf{q}) = 2\pi e^2 \tanh(d|\mathbf{q}|) / (4\pi\epsilon_0\epsilon|\mathbf{q}|)$, d is the gate-to-sample distance and here we take $d = 2a_M$. After simplification, we obtain the following forms for practical computational use

$$t_{im,jn}^{\sigma} = \frac{1}{N} \sum_{\mathbf{k}} e^{i\mathbf{k}\cdot(\mathbf{R}_i - \mathbf{R}_j)} \left[U(\mathbf{k}) \begin{pmatrix} \varepsilon_{1\mathbf{k}}^{\sigma} & 0 \\ 0 & \varepsilon_{2\mathbf{k}}^{\sigma} \end{pmatrix} U^{\dagger}(\mathbf{k}) \right]_{mn} \quad (6)$$

$$U_{im,jn} = \frac{1}{N} \sum_{\mathbf{q}} \frac{V(\mathbf{q})}{\Omega} M_m^*(\mathbf{q}) M_n(\mathbf{q}) e^{i\mathbf{q} \cdot (\mathbf{R}_i - \mathbf{R}_j)} \quad (7)$$

where $\Omega = \sqrt{3}a_M^2/2$ and $M_n(\mathbf{q})$ takes the form

$$M_n(\mathbf{q}) = \frac{1}{N} \sum_{\mathbf{k}\mathbf{k}'\mathbf{G}\mathbf{G}'} b_{n\mathbf{k}l}^{\mathbf{G}*} b_{n\mathbf{k}'l}^{\mathbf{G}'} \delta_{\mathbf{k}+\mathbf{G},\mathbf{k}'+\mathbf{G}'+\mathbf{q}} \quad (8)$$

where $b_{n\mathbf{k}l}^{\mathbf{G}}$ is the component of $\chi_{\mathbf{k}l}^{\mathbf{G}}$ in $\varphi_{n\mathbf{k}}(\mathbf{r})$, that is, $\varphi_{n\mathbf{k}}(\mathbf{r}) = \sum_{\mathbf{G}} \sum_{l=b,t} b_{n\mathbf{k}l}^{\mathbf{G}} \chi_{\mathbf{k}l}^{\mathbf{G}}(\mathbf{r})$.

Band-basis exact diagonalization

For a general free tight-binding Hamiltonian in the honeycomb lattice $H_0 = \sum_{ijmn\sigma} c_{im\sigma}^\dagger h_{im,jn}^\sigma c_{jn\sigma}$, where i, j is the site index, $m, n = A, B$ is the sublattice index and $\sigma = \uparrow, \downarrow$ is the spin index, we can derive its band basis by a successive Fourier transformation and diagonalization

$$H_0 = \sum_{kmn\sigma} c_{km\sigma}^\dagger h_{mn}^\sigma(\mathbf{k}) c_{kn\sigma} = \sum_{\mathbf{k}\mu\sigma} \alpha_{\mathbf{k}\mu\sigma}^\dagger \varepsilon_\mu^\sigma(\mathbf{k}) \alpha_{\mathbf{k}\mu\sigma} \quad (9)$$

where $\mu = l, u$ is the band index with l, u for lower/upper band and $\alpha_{\mathbf{k}\mu\sigma} = \sum_n U_{n\mu}^{\sigma*}(\mathbf{k}) c_{kn\sigma}$, $U(\mathbf{k})$ is the unitary matrix to diagonalize Hamiltonian H . The Hubbard term $H_U = U \sum_{in} n_{in\uparrow} n_{in\downarrow}$ can be expressed in term of band basis as follow

$$H_U = \frac{U}{N} \sum_{nkk'q} \sum_{\mu\nu} U_{n\mu}^{\uparrow*}(k+q) U_{n\mu'}^\uparrow(k) U_{n\nu}^{\downarrow*}(k'-q) U_{n\nu'}^\downarrow(k') \alpha_{k+q\mu\uparrow}^\dagger \alpha_{k\mu'\uparrow} \alpha_{k'-q\nu\downarrow}^\dagger \alpha_{k'\nu'\downarrow} \quad (10)$$

In the $\Delta S_z = -1$ space spanned by $|\mathbf{k}, \mathbf{q}, \mu\rangle = \alpha_{\mathbf{k}+\mathbf{q}\mu\downarrow}^\dagger \alpha_{\mathbf{k}l\uparrow} |\text{GS}\rangle$, where $|\text{GS}\rangle = \prod_{\mathbf{k} \in 1\text{BZ}} \alpha_{\mathbf{k}l}^\dagger |0\rangle$, matrix elements of H_0 and H_U has the following form

$$\langle \mathbf{k}, \mathbf{q}, \mu | H_0 | \mathbf{k}', \mathbf{q}, \nu \rangle = \left[\varepsilon_\mu^\downarrow(\mathbf{k} + \mathbf{q}) - \varepsilon_l^\uparrow(\mathbf{k}) \right] \delta_{\mathbf{k}\mathbf{k}'} \delta_{\mu\nu} \quad (11)$$

$$\begin{aligned} \langle \mathbf{k}, \mathbf{q}, \mu | H_U | \mathbf{k}', \mathbf{q}, \nu \rangle &= \frac{U}{N} \sum_{n\mathbf{k}''} |U_{nl}^\uparrow(\mathbf{k}'')|^2 U_{n\mu}^{\downarrow*}(\mathbf{k} + \mathbf{q}) U_{n\nu}^\downarrow(\mathbf{k} + \mathbf{q}) \delta_{\mathbf{k}\mathbf{k}'} \\ &\quad - \frac{U}{N} \sum_n U_{nl}^{\uparrow*}(\mathbf{k}') U_{nl}^\uparrow(\mathbf{k}) U_{n\mu}^{\downarrow*}(\mathbf{k} + \mathbf{q}) U_{n\nu}^\downarrow(\mathbf{k}' + \mathbf{q}) \end{aligned} \quad (12)$$

The total Hamiltonian $H = H_0 + H_U$ can be written in terms of scattering processes

$$\begin{aligned} H(\mathbf{q}) &= \sum_{\mathbf{k}\mu} \left[\varepsilon_\mu^\downarrow(\mathbf{k} + \mathbf{q}) - \varepsilon_l^\uparrow(\mathbf{k}) \right] |\mathbf{k}, \mathbf{q}, \mu\rangle \langle \mathbf{k}, \mathbf{q}, \mu| \\ &\quad + \frac{U}{N} \sum_{\mathbf{k}\mu\nu} \sum_{n\mathbf{k}''} |U_{nl}^\uparrow(\mathbf{k}'')|^2 U_{n\mu}^{\downarrow*}(\mathbf{k} + \mathbf{q}) U_{n\nu}^\downarrow(\mathbf{k} + \mathbf{q}) |\mathbf{k}, \mathbf{q}, \mu\rangle \langle \mathbf{k}, \mathbf{q}, \nu| \\ &\quad - \frac{U}{N} \sum_{\mathbf{k}\mathbf{k}'\mu\nu} \sum_n U_{nl}^{\uparrow*}(\mathbf{k}') U_{nl}^\uparrow(\mathbf{k}) U_{n\mu}^{\downarrow*}(\mathbf{k} + \mathbf{q}) U_{n\nu}^\downarrow(\mathbf{k}' + \mathbf{q}) |\mathbf{k}, \mathbf{q}, \mu\rangle \langle \mathbf{k}', \mathbf{q}, \nu| \end{aligned} \quad (13)$$

For a general Hamiltonian matrix $h_{\mathbf{k}} = \sum_i h_i(\mathbf{k}) \sigma^i$, where σ^i is the Pauli matrix, the unitary matrix has the form $|U_{nl}(\mathbf{k})|^2 = \frac{1}{2} \left(1 \pm \frac{h_z(\mathbf{k})}{h(\mathbf{k})} \right)$, where $h(\mathbf{k}) = \sqrt{h_x^2(\mathbf{k}) + h_y^2(\mathbf{k}) + h_z^2(\mathbf{k})}$ and \pm for $n = A, B$. If the system is invariant under inversion $P : c_{\mathbf{k}A} \rightarrow c_{-\mathbf{k}B}, c_{\mathbf{k}B} \rightarrow c_{-\mathbf{k}A}$, then we have $h_x(-\mathbf{k}) = h_x(\mathbf{k}), h_{y,z}(-\mathbf{k}) = -h_{y,z}(\mathbf{k})$, so that $\sum_{\mathbf{k}} |U_{nl}(\mathbf{k})|^2 = \frac{N}{2}$ and the second term in Eq.12 is $\frac{U}{2} \sum_{\mathbf{k}\mu} |\mathbf{k}, \mathbf{q}, \mu\rangle \langle \mathbf{k}, \mathbf{q}, \mu|$. We notice that $c_{\mathbf{k}+\mathbf{q}n\downarrow}^\dagger c_{\mathbf{k}n\uparrow} |\text{GS}\rangle = \sum_{\mu} U_{n\mu}^{\downarrow*}(\mathbf{k} + \mathbf{q}) U_{nl}^\uparrow(\mathbf{k}) |\mathbf{k}, \mathbf{q}, \mu\rangle$ and by defining $|\mathbf{q}, n\rangle \equiv \sum_{\mathbf{k}} c_{\mathbf{k}+\mathbf{q}n\downarrow}^\dagger c_{\mathbf{k}n\uparrow} |\text{GS}\rangle$, the third term can be simplified to be $\frac{U}{N} \sum_n |\mathbf{q}, n\rangle \langle \mathbf{q}, n|$. Finally, the total Hamiltonian has the following compact form

$$H(\mathbf{q}) = \sum_{\mathbf{k}\mu} \left[\frac{U}{2} + \varepsilon_\mu^\downarrow(\mathbf{k} + \mathbf{q}) - \varepsilon_l^\uparrow \right] |\mathbf{k}, \mathbf{q}, \mu\rangle \langle \mathbf{k}, \mathbf{q}, \mu| - \frac{U}{N} \sum_n |\mathbf{q}, n\rangle \langle \mathbf{q}, n| \quad (14)$$

When an staggered chemical potential is applied, the inversion symmetry is explicitly broken so the $\frac{U}{2}$ in Eq.14 should be replaced by the form in Eq.13.

Magnetic effective model

Motivated by the fact that $|\mathbf{q}, n\rangle = \sum_i e^{i\mathbf{q}\cdot\mathbf{R}_i} c_{in\downarrow}^\dagger c_{in\uparrow} |\text{GS}\rangle$ which is a collection of onsite spin flip projecting on the itinerant FM ground state, we focus on the space spanned by $|\beta_{in}^\dagger\rangle \equiv c_{in\downarrow}^\dagger c_{in\uparrow} |\text{GS}\rangle$ which forms an orthogonal basis

$$\langle \text{GS} | \beta_{im} \beta_{jn}^\dagger | \text{GS} \rangle = \frac{1}{N} \sum_{\mathbf{k}} |U_{nl}^\dagger(\mathbf{k})|^2 \delta_{ij} \delta_{mn} \quad (15)$$

Under the inversion symmetry, $\langle \text{GS} | \beta_{in} \beta_{jn}^\dagger | \text{GS} \rangle = \frac{1}{2} \delta_{ij} \delta_{mn}$ so that $\{\sqrt{2} \beta_{in}^\dagger | \text{GS} \rangle\}$ forms an orthonormal basis. For convenience, we take the operators to be $\tilde{\beta}_{in}^\dagger \equiv \beta_{in}^\dagger | \text{GS} \rangle \langle \text{GS} |$ and the hopping parameters to be $t_{im,jn}^{\text{bound}} \equiv \langle \text{GS} | \beta_{im} H \beta_{jn}^\dagger | \text{GS} \rangle$ up to a normalized factor. Notice that the onsite spin flip do not produce double occupation so $\langle \text{GS} | \beta_{im} H \beta_{jn}^\dagger | \text{GS} \rangle = \langle \text{GS} | \beta_{im} H_0^\uparrow \beta_{jn}^\dagger | \text{GS} \rangle + \langle \text{GS} | \beta_{im} H_0^\downarrow \beta_{jn}^\dagger | \text{GS} \rangle$, by dividing the ground into spin- \uparrow itinerant FM and spin- \downarrow vacuum, i.e., $|\text{GS}\rangle = |\text{IFM}, \uparrow\rangle \times |0, \downarrow\rangle$, $t_{im,jn}^{\text{bound}}$ can be expressed as

$$\begin{aligned} t_{im,jn}^{\text{bound}} &= \langle \text{IFM}, \uparrow | c_{im\uparrow}^\dagger H_0^\uparrow c_{jn\uparrow} | \text{IFM}, \uparrow \rangle \langle 0, \downarrow | c_{im\downarrow} c_{jn\downarrow}^\dagger | 0, \downarrow \rangle \\ &+ \langle \text{IFM}, \uparrow | c_{im\uparrow}^\dagger c_{jn\uparrow} | \text{IFM}, \uparrow \rangle \langle 0, \downarrow | c_{im\downarrow} H_0^\downarrow c_{jn\downarrow}^\dagger | 0, \downarrow \rangle \end{aligned} \quad (16)$$

obviously, $\langle 0, \downarrow | c_{im} c_{jn}^\dagger | 0, \downarrow \rangle = \delta_{ij} \delta_{mn}$ and $\langle 0, \downarrow | c_{im\downarrow} H_0^\downarrow c_{jn\downarrow}^\dagger | 0, \downarrow \rangle = t_{im,jn,e}^\downarrow$ is the hopping of the spin- \downarrow electron. By direct calculation, we finally obtain

$$t_{im,jn}^{\text{bound}} = M_{im} \delta_{ij} \delta_{mn} + \tilde{t}_{im,jn,h}^\uparrow \cdot t_{im,jn,e}^\downarrow \quad (17)$$

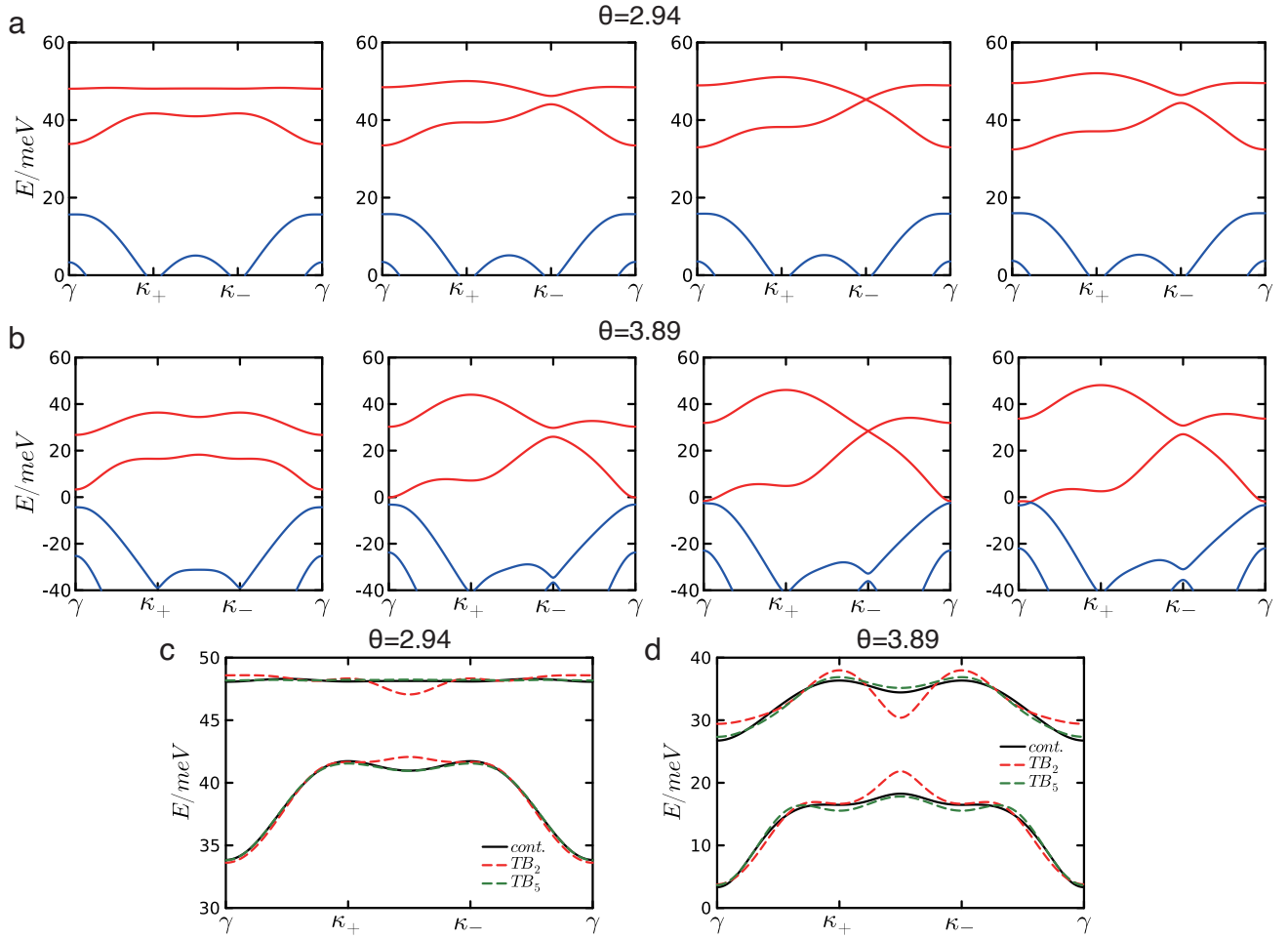
where

$$M_{im} = \frac{1}{N} \sum_{\mathbf{k}} |U_{ml}^\dagger(\mathbf{k})|^2 \sum_{\mathbf{k}' \neq \mathbf{k}} \varepsilon_l^\dagger(\mathbf{k}') \quad (18)$$

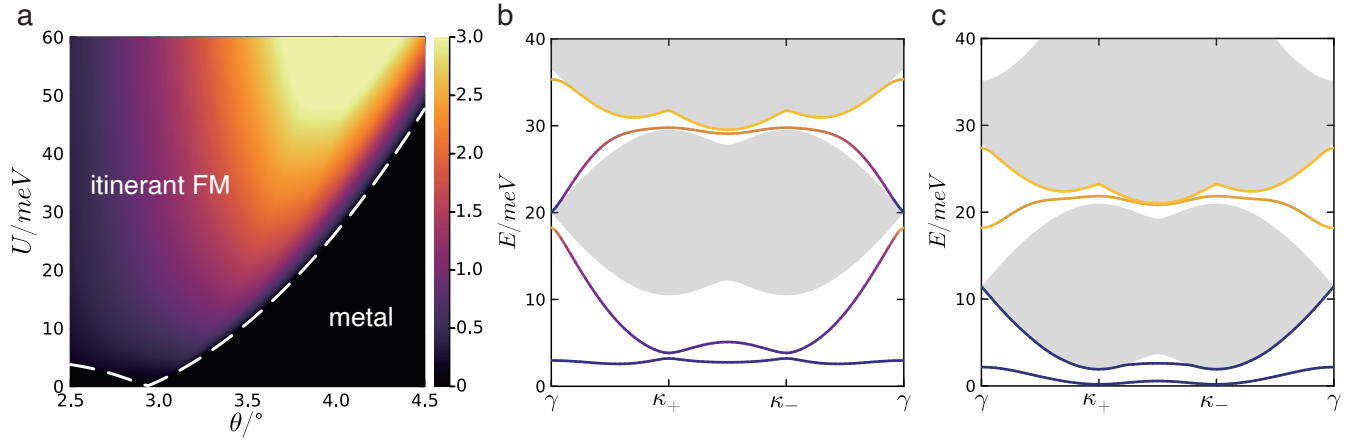
$$\tilde{t}_{im,jn,h}^\uparrow = \frac{1}{N} \sum_{\mathbf{k}} e^{-i\mathbf{k}\cdot(\mathbf{R}_i - \mathbf{R}_j)} U_{ml}^{\dagger*}(\mathbf{k}) U_{nl}^\dagger(\mathbf{k}) \quad (19)$$

where $\tilde{t}_{im,jn,h}^\uparrow$ can be regarded as the effective hopping of the spin- \uparrow hole. From the above expression one can see that the hopping of the magnon is the product of the electron and hole, and its topology is directly inherited from the electron band topology. If we have a ground state with the two spin- \uparrow bands fully occupied, i.e., $|\tilde{\text{GS}}\rangle \equiv \prod_{\mathbf{k} \in \text{1BZ}} \alpha_{\mathbf{k}u\uparrow}^\dagger \alpha_{\mathbf{k}l\uparrow}^\dagger |0\rangle$ which is in fact a ferromagnetism with one spin- \uparrow electron per site, one can that $\langle \text{IFM}, \uparrow | c_{im\uparrow}^\dagger c_{jn\uparrow} | \text{IFM}, \uparrow \rangle = 0$ for $i \neq j$, so that the topology of magnon in local spin system can not be directly inherited from the electron band topology, at least in first order. From another perspective, $\langle \text{IFM}, \uparrow | c_{im\uparrow}^\dagger c_{jn\uparrow} | \text{IFM}, \uparrow \rangle$ is in fact the charge fluctuation of the ferromagnetic ground state, which is nonzero only in itinerant system but vanishes in local spin systems.

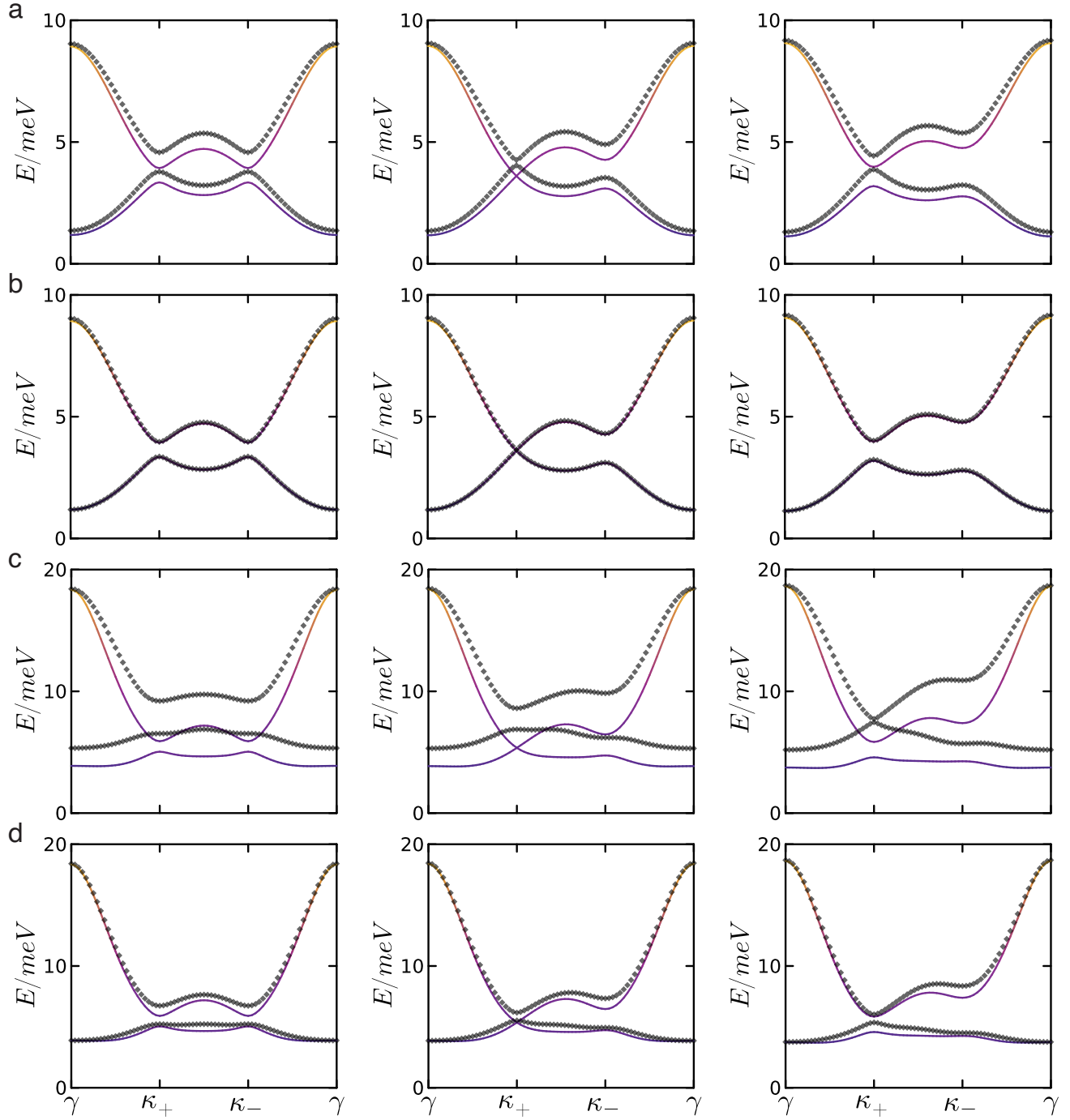
EXTENDED DATA FIGURES



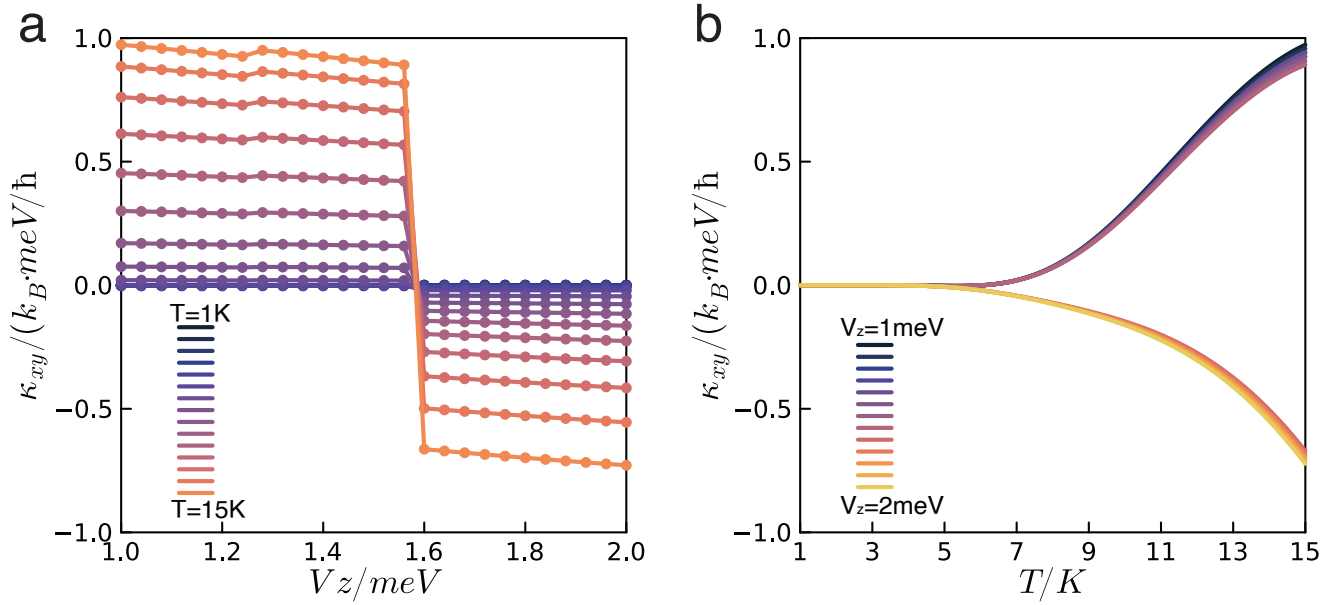
Extended Data Fig. 1 — **a.** Electron bands derived by continuum model at $\theta = 2.94^\circ$, $V_z = (0, 5, 7.58, 10)$ meV (from left to right) and **b.** $\theta = 3.89^\circ$, $V_z = (0, 20, 24.99, 30)$ meV. **c.** Comparison of the electron bands derived by continuum model and tight-binding model at $\theta = 2.94^\circ$, $V_z = 0$ and **d.** $\theta = 3.89^\circ$, $V_z = 0$



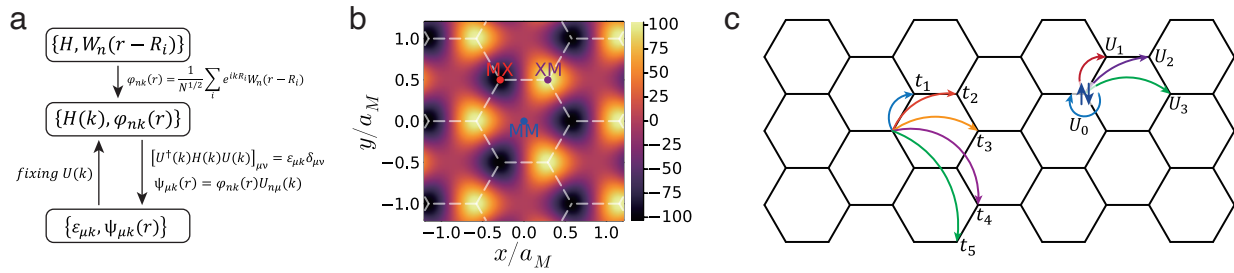
Extended Data Fig. 2 — **a.** Phase diagram of itinerant FM and metal at $V_z = 0$. The color represents the minimum energy of the magnons E_{\min} and the region where $E_{\min} < 0$ is uniformly colored by black. Magnon band structures at **b.** $(\theta, U) = (3.89^\circ, 40\text{meV})$ and **c.** $(\theta, U) = (3.89^\circ, 22.9\text{meV})$, respectively. The latter presents a signature of the instability of the itinerant FM.



Extended Data Fig. 3 — **a.** Magnon dispersion at $\theta = 2.94^\circ$ derived by ED in $\Delta S_z = -1$ space and magnetic effective model in B_2 space, and **b.** in B_4 space, from left to right $V_z = (0, 0.85, 2)\text{meV}$. **c.** Magnon dispersion at $\theta = 3.89^\circ$ derived by ED in $\Delta S_z = -1$ space and magnetic effective model in B_2 space, and **d.** in B_4 space, from left to right $V_z = (0, 1.56, 4)\text{meV}$. The solid lines represent the ED results which share the same color bar as that in the main text. The diamonds represent the dispersion from the magnetic effective model. All results are derived at $U = 80\text{meV}$.



Extended Data Fig. 4 — **a.** Thermal Hall conductance at $(\theta, U) = (3.89^\circ, 80\text{meV})$ by varying V_z at different temperature T and **b.** by varying T at different V_z .



Extended Data Fig. 5 — **a.** Sketch of the generation of tight-binding model. The point is to fixing $U(k)$. **b.** Distribution of moiré potential (in unit of 1meV) $\Delta_z = (\Delta_b - \Delta_t)/2$. Δ_b/t reaches its maximum at XM/MX stacking region, respectively. **c.** Hopping terms and interactions.